Nuclear Inst. and Methods in Physics Research B 451 (2019) 10–13

Contents lists available at ScienceDirect

Nuclear Inst. and Methods in Physics Research B

journal homepage: www.elsevier.com/locate/nimb

Nitrogen ion implantation into pure iron for formation of surface nitride layer

Tianyi Chen[a], Elizabeth Castanon[b], Jonathan G. Gigax[c], Hyosim Kim[b], Robert Balerio[b], Jiangyuan Fan[b], F.A. Garner[b], Lin Shao[b,*]

[a] School of Nuclear Science and Engineering, Oregon State University, Corvallis, OR 97331, USA
[b] Department of Nuclear Engineering, Texas A&M University, TX 77843, USA
[c] Los Alamos National Lab, Los Alamos, NM 87545, USA

ARTICLE INFO

Keywords:
Ion implantation
Nitride

ABSTRACT

Low energy N ion implantation into pure Fe was performed to study $Fe_{1-x}N_x$ formation under various ion irradiation conditions. It was shown that after the room-temperature implantation the amount of N introduction reaches a saturation at about 42% atomic density. Increasing N fluences further does not increase N levels. For the N saturated layer, adding post-irradiation annealing causes N out-diffusion at 300 °C and higher temperatures. On the other hand, N implantation at elevated temperatures does not provide extra thermal stability. Transmission electron microscopy and localized diffraction analysis show that the metastable N saturated layer contains a mixture of Fe_3N and FeN_2.

1. Introduction

In reactor harsh environments involving high stress, high corrosion and high irradiation damage, fuel cladding materials experience severe structural changes and degradation, which impacts not only their lifespan but also reactor safety and reliability [1]. Development of advanced fuel cladding materials is critical for both life extension of present reactors and advanced reactor designs with even harsher operation conditions. Numerous studies have shown that a surface nitride layer can be used to increase hardness, wear resistance, oxidation resistance, and corrosion resistance of nuclear materials [2–5]. Previous corrosion studies on AISI 304 austenitic steels have shown significant pitting corrosion in untreated samples [2]. In comparison, nitrided steels obtained from plasma nitridation have shown superior corrosion resistance due to the formation of an adhering anodic passivation layer [2]. Nitridation also significantly enhances wear resistance, due to the enhanced hardness and nitridation-introduced compressive stresses on the surface, which tend to close existing microcracks and further impede their formation [3–5]. These early studies strongly suggest the great potential of nitridation techniques for enhancing structural integrity of fuel cladding in both reactor environments and spent fuel storage.

Traditional nitridation, however, involves large energy deposition on the metal surface. Under high energy deposition, local melting may occurs [6]. The local heating may lead to phase and microstructure instability, diverting the alloys from their optimized condition. The local heating is related to nitrogen flux and bias. Thus temperature is not often a controllable and independent variable. Low energy ion implantation, on the other hand, can be used as one method to minimize such energy deposition, with temperature as one adjustable variable. For this study, we used pure Fe as a model material to simulate Fe-based stainless steels. The results of this study can benefit optimization of the plasma nitridation process, such as selection of voltage bias, power deposition and nitridation periods.

2. Experimental procedure

Fe of high purity (99.995%) was mechanically polished and electronically polished to pieces of 1 cm × 1 cm × 1 mm dimension, and implanted with 40 keV N ions at different temperatures of 25 °C, 100 °C, 300 °C, and 500 °C, with different fluences of N ions of 1×10^{17}, 5×10^{17}, 1×10^{18}, and 2×10^{18} atoms/cm^2. The vacuum during ion irradiation and annealing were both kept at 1×10^{-6} torr. Selected samples were further annealed at temperatures of 100 °C, 300 °C, and 500 °C for about 6 h each. Annealing was performed immediately after the N ion implantation without breaking the vacuum. Such post-implantation annealing was used to further evaluate stability of the nitride layers. All samples were characterized using the Rutherford

* Corresponding author.
E-mail address: lshao@tamu.edu (L. Shao).

https://doi.org/10.1016/j.nimb.2019.04.033
Received 15 September 2018; Received in revised form 10 April 2019; Accepted 11 April 2019
Available online 01 May 2019
0168-583X/ © 2019 Elsevier B.V. All rights reserved.

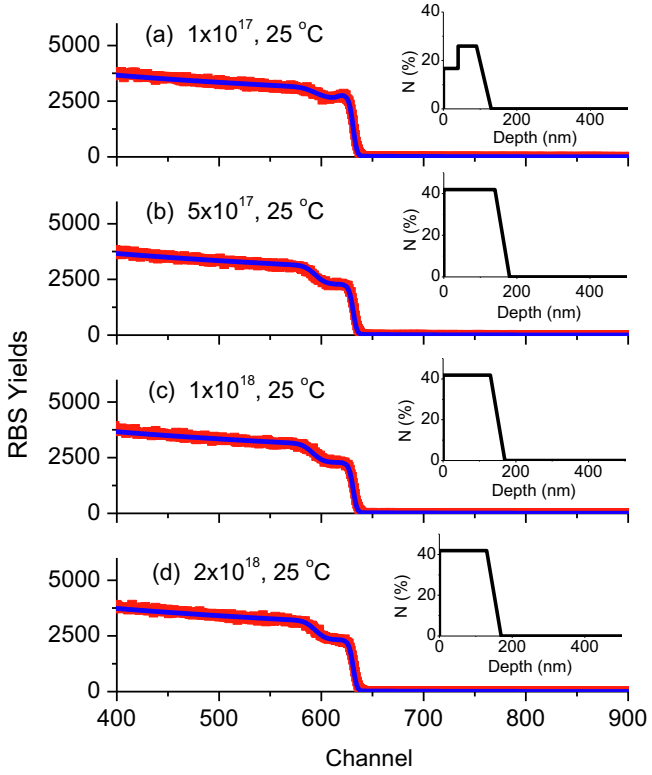


Fig. 1. Experimental RBS spectra (red) and simulated RBS spectra (blue) for Fe implanted at room temperature with N fluences of (a) 1×10^{17}, (b) 5×10^{17}, (c) 1×10^{18}, and (d) 2×10^{18} atoms/cm^2. The insets are corresponding N depth distributions obtained from best fitting. (For interpretation of the references to color in this figure legend, the reader is referred to the web version of this article.)

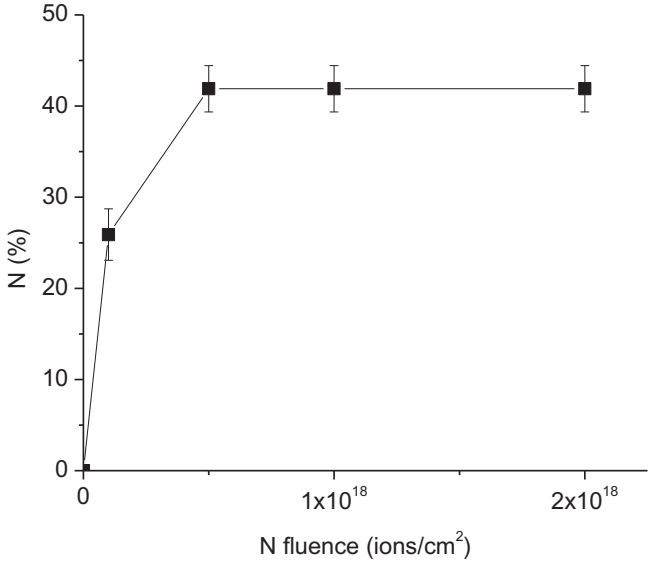


Fig. 2. N concentrations (atomic percentage) in the N peak region as a function of N fluences implanted at room temperature. The data is extracted from Fig. 1.

backscattering (RBS) technique with a 2 MeV helium analysis beam. A semiconductor detector of 20 keV energy resolution was positioned 165° away from the beam direction. The RBS spectra were simulated using RUMP software [7] to extract the nitrogen profiles. Some of the implanted samples were characterized using transmission electron microscopy (TEM) using a Technai F20 Supertwin TEM operated at

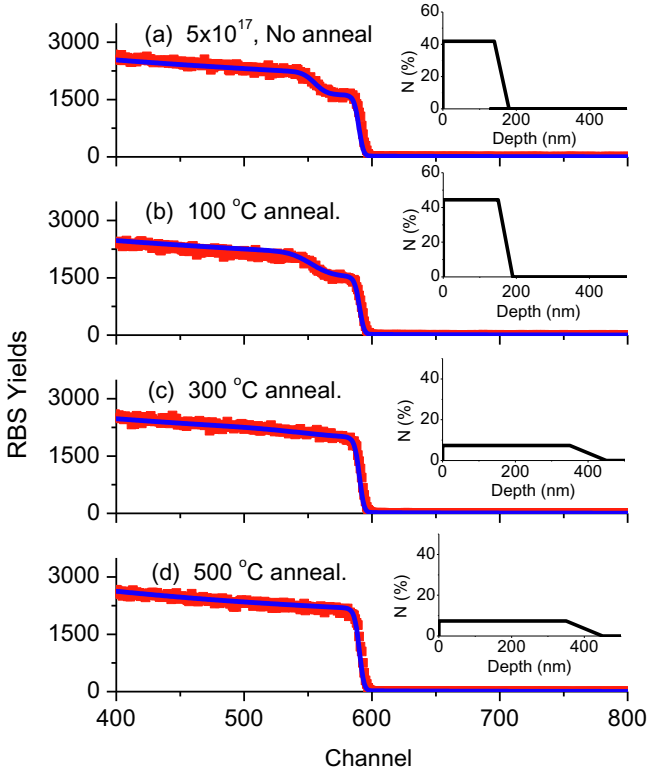


Fig. 3. Experimental RBS spectra (red) and simulated RBS spectra (blue) for Fe implanted at room temperature to a fluence of 5×10^{17} atoms/cm^2 (a) before annealing and after annealing at temperatures of (b) 100 °C, (c) 300 °C, and (d) 500 °C, respectively. The insets are corresponding N depth distributions obtained from best fitting. (For interpretation of the references to color in this figure legend, the reader is referred to the web version of this article.)

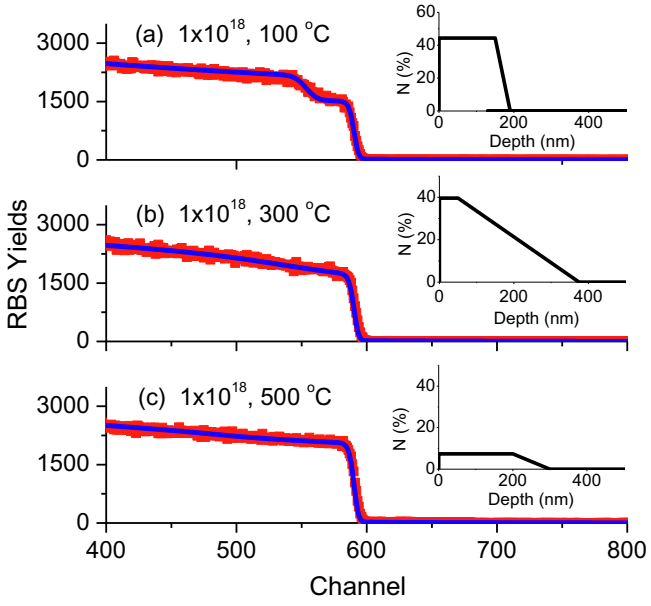


Fig. 4. Experimental RBS spectra (red) and simulated RBS spectra (blue) for Fe implanted to a fixed fluence of 5×10^{17} atoms/cm^2 and at implantation temperatures of (a) 100 °C, (b) 300 °C, and (c) 500 °C. The insets are corresponding N depth distributions obtained from best fitting.

200 kV. Both traditional TEM and high resolution TEM (HRTEM) were performed. TEM specimens were prepared employing the focused-ion-beam (FIB) liftout technique, using a Tescan LYRA-3 FIB.

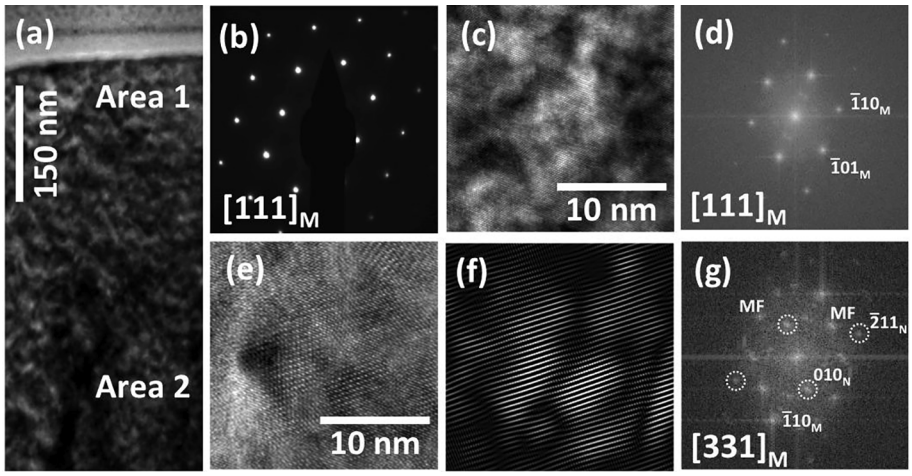


Fig. 5. (a) A cross sectional TEM view of 1×10^{18} N-implanted Fe at room temperature with "area 1" referring to N-implanted region within the N projected range and "area 2" referring to an un-implanted region beyond the N projected range, and (b) diffraction pattern of area 2, and (c) HRTEM obtained from area 2 at [1 1 1] matrix zone axis, and (d) FFT pattern of (c), and (e) HRTEM obtained from area 1 at [3 3 1] matrix zone axis, and (f) inverse FFT pattern of (e), and (g) indexed FFT pattern of (e) with circles referring to the diffraction spots used to construct (f). MF in (g) labels the spots corresponding to the Moiré fringes.

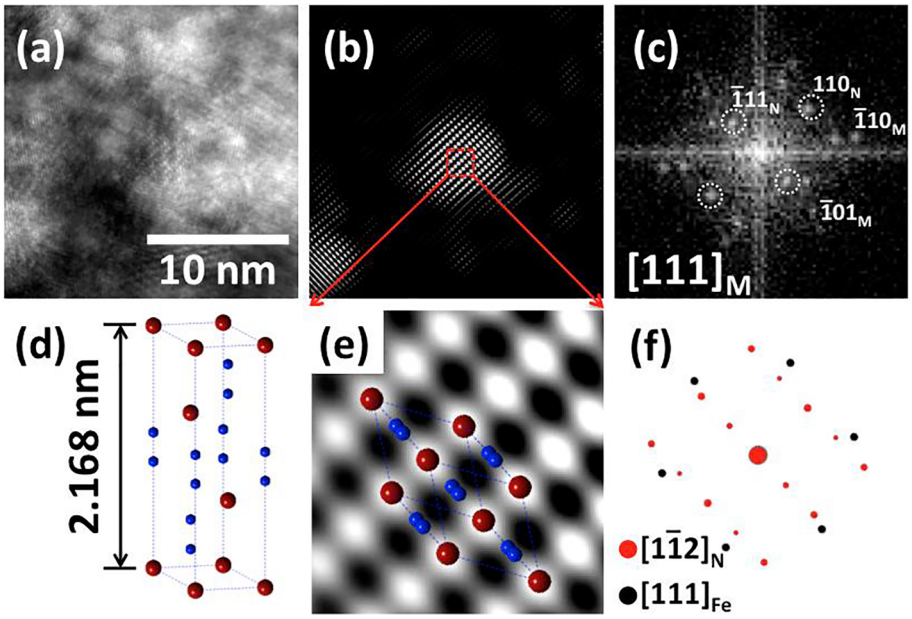


Fig. 6. (a) A high resolution cross-sectional TEM view of 1×10^{18} N-implanted Fe at room temperature, obtained from N-implanted region, and (b) the corresponding inverse FFT pattern and (c) the corresponding indexed FFT pattern with circled spots used to construct (b), and (d) schematics of FeN_2 crystal structure with blue color referring to N atoms and red color referring to Fe atoms, and (e) the comparison of inverse FFT pattern and projected view of FeN_2 crystal structure, and (f) simulated diffraction patterns.

3. Results and discussions

Fig. 1a–d show the RBS spectra of Fe samples after 40 keV N implantation to fluences of 1×10^{17}, 5×10^{17}, 1×10^{18}, and 2×10^{18} atoms/cm^2, respectively. The solid lines are the corresponding RBS fittings by RUMP. As shown in Fig. 1a, the lowest fluence of 1×10^{17} atoms/cm^2 leads to a buried N peak of about 26% N atomic density at depths from 40 nm to 90 nm. The peak depth location agrees with the N implant peak location at about 50 nm, calculated by using the Monte Caro simulation code of SRIM (The Stopping and Range of Ions in Matter) [8]. In the near-surface region shallower than 40 nm, the N concentration is about 17%. Increasing N fluence to 5×10^{17} atoms/cm^2 leads to a higher N concentration of 42%, uniformly distributed from the surface to 140 nm, as shown in Fig. 1b. Increasing N fluences to even higher values of 1×10^{18} and 2×10^{18} atoms/cm^2, as shown in Fig. 1c and d, however, does not provide additional N introduction. The N concentration is saturated at 42%. RBS spectra do not show a diffusion tail into the bulk direction, primarily due to low thermal budget annealing from room temperature implantation. Extra N atoms are believed to diffuse out from the Fe surface. Fig. 2 summarizes the amount N that stayed in the Fe matrix as a function of N ion fluence, which clearly shows that the N saturation was reached at an fuence of 5×10^{17} N atoms/cm^2. The error bars in Fig. 2 are estimated by RBS spectral fitting, and determined by adjusting N concentrations over a range beyond which the fitted curves begin to have noticeable deviation from experimental spectra.

On the other hand, the N-saturated Fe layer shows poorer thermal stability during post-implantation annealing. Fig. 3a–d show RBS spectra and N profile fitting obtained before and after annealing at 100 °C, 300 °C, and 500 °C. Before thermal annealing, the N profile is box-like and has a flat N concentration at 42% (Fig. 3a). After annealing at 100 °C, there is no visible profile change, suggesting that the formed $Fe_{1-x}N_x$ phase is thermally stable. (Fig. 3b). After annealing at 300 °C, the N concentration drops to about 7.5% with the profile width increased to 350 nm (Fig. 3c). Annealing at 500 °C does not further change the N profiles as shown in Fig. 3d.

N implantation at elevated temperature does not provide extra thermal stability. Fig. 4a–c show RBS spectra obtained from implantation temperatures of 100 °C, 300 °C, and 500 °C, respectively. All N implantation was to the same fluence of 1×10^{18} atoms/cm^2. As shown in Fig. 4a, the irradiation at 100 °C creates a N-saturated layer of 150 nm width and 44% N concentration, which is similar to the room temperature N ion irradiation. For a higher temperature of 300 °C, as shown in Fig. 4b, the N peak concentration is slightly reduced to 40%, and the N width is narrowed down to 50 nm with a long diffusion tail into the bulk. For the highest temperature of 500 °C, the N peak

concentration drops down to 7.4%. Similar to observations from post-implantation annealing experiment, the N-saturated layer is thermally dissociated and diffuses out at the temperatures of 300 °C and above.

TEM characterization provides atomic scale details of nitride formation in N-implanted region. Fig. 5a shows a cross sectional view of the Fe implanted at room temperature and to a fluence 1×10^{18} atoms/cm^2. The marked "area 1" refers to the N-implanted area, while "area 2" refers to the implantation-free region beyond N projected range. Fig. 5b shows a diffraction pattern collected from area 2 at the [1 1 1] zone axis of the matrix. The diffraction pattern confirms the bcc structure of bulk Fe. Fig. 5c is a high resolution TEM micrograph from the same region and Fig. 5d is the corresponding fast-Fourier-transformation (FFT) pattern, which is indexed to show the agreement with bcc Fe. For region 1 (implanted region), Fig. 5e is a high resolution TEM micrograph obtained at [3 3 1] zone axis, which shows nano-precipitates embedded in the bcc ion matrix. Fig. 5f is inverse FFT pattern which suggests coherency of crystal alignments between nano-precipitates and the Fe matrix. Fig. 5g is the corresponding FFT pattern providing evidence that the precipitates are Fe_3N phase [9]. Superimposed with bcc diffraction spots are FFT spots indexed as (0 1 0) and $(\bar{2}\ 1\ 1)$ of Fe_3N phase. The index further shows an $[1\ 0\ 1]_{\text{nitride}}//[3\ 3\ 1]_{\text{matrix}}$ coherency.

In addition to Fe_3N, we identify another nitride phase that suggests the theoretically predicted R3m structure of FeN_2 [10]. Evidence is provided in Fig. 6a–f. Fig. 6a is a HRTEM obtained at the [1 1 1] matrix zone axis from area 1, which shows a precipitate having d spacings of 0.49 nm and 0.29 nm. Fig. 6b is the inverse FFT image and Fig. 6c is the indexed FFT patterns. The two spots corresponding to the 0.49 and 0.29 nm d spacing were indexed as $(\bar{1}\ 1\ 1)$ and (110) of the FeN_2. Circled diffraction spots of Fig. 6c are used to construct Fig. 6b. Fig. 6d schematically shows the crystal structure of FeN_2 [10]. Fig. 6e compares the inverse FFT image and the corresponding projected view of FeN_2 atom positions. Fig. 6f is the simulated diffraction patterns of bcc Fe at [1 1 1] zone axis and FeN_2 at $[1\ \bar{1}\ 2]$ zone axis. The agreement between Fig. 6f and c is evidence of the formation of FeN_2 phases. The lattice parameter of FeN_2 measured from the present study is 8% larger than the 2.0075 nm predicted with early first principle calculations [10].

4. Conclusion

Low energy N ion implantation provides an efficient way to evaluate nitride phase formation, and phase stability. The knowledge can be used to specify plasma nitridation parameters. The present study show that nitride phases formed in pure Fe after traditional N ion implantation in general are not stable, regardless of whether annealing is performed during ion implantation or not.

Acknowledgement

The study is supported by U.S. Department of Energy through NEUP program, grant number 15-8521.

References

[1] T. Allen, J. Busby, M. Meyer, D. Petti, Mater. Today 13 (2010) 12.
[2] M.E. Chabica, D.L. Williamson, R. Wei, P.J. Wibur, Surface Coat. Technol. 51 (1992) 24–29.
[3] W. Liang, X. Bin, Y. Zhiwei, S. Yaqin, Surface Coat. Technol. 130 (2000) 304–308.
[4] L. Shen, L. Wang, Y. Wang, C. Wang, Surface Coat. Technol. 204 (2010) 3222–3227.
[5] W. Liang, Appl. Surface Sci. 211 (2003) 308–314.
[6] K. Taweesub, P. Visuttipitukul, S. Tungkasmita, B. Paosawatyanyong, Surface Coat. Technol. 204 (2010) 3091–3095.
[7] L.R. Doolittle, Nucl. Instrum. Meth. B 9 (1985) 344–351.
[8] J.F. Ziegler, M.D. Ziegler, J.P. Biersack, Nucl. Instrum. Meth. B 268 (2010) 1818–1823.
[9] K.H. Jack, Acta Cryst. 5 (1952) 404.
[10] M. Wessel, R. Dronskowski, Chem.-A Eur. J. 17 (2011) 2598–2603.